

Robustness Assessment of Static Structures for Efficient Object Handling

Philippe Nadeau and Jonathan Kelly

Abstract—This work establishes a solution to the problem of assessing the robustness of multi-object assemblies to external forces. Our physically-grounded approach handles arbitrary static structures made from rigid objects of any shape and mass distribution without relying on heuristics or approximations. The result is a method that provides a foundation for autonomous robot decision-making when interacting with objects in frictional contact. Our strategy decouples slipping from toppling, enabling independent assessments of these two phenomena, with a shared robustness representation being key to combining the results into an accurate robustness assessment. Our algorithms can be used by motion planners to produce efficient assembly transportation plans, and by object placement planners to select poses that improve the strength of an assembly. Compared to prior work, our approach is more generally applicable than commonly used heuristics and more efficient than dynamics simulations.

Index Terms—Assembly, Stability, Manipulation Planning

I. INTRODUCTION

ASSESSING the capacity of multi-object assemblies to withstand external forces is crucial for enabling robots to make informed decisions in real-world environments, where autonomy hinges on accurate and reliable world models. Mobile robots efficiently traversing cluttered environments [1, 2], robotic manipulators planning grasps [3, 4, 5] or placing objects [6, 7, 8], autonomous construction robots [9, 10], and robots in many other contexts all need to answer the question: *What forces can objects withstand before becoming unstable?* Answering this question accurately enables a robot to safely interact with its surroundings and make informed decisions when handling and manipulating objects.

This work proposes a novel method for evaluating the *robustness* of rigid object assemblies, that is, their capacity to withstand external forces, as pictured in Fig. 1. Specifically, we address the problem of determining how external forces impact the robustness of an assembly of rigid bodies in frictional contact and static equilibrium. We propose and evaluate algorithms that, given the known but arbitrary poses, inertial parameters, and friction coefficients of bodies in an assembly, assess the assembly’s robustness and determine how applied forces can improve its stability. We believe that our solution to the aforementioned problem can provide a foundation for autonomous decision-making when interacting with objects in frictional contact. To highlight potential applications of our method, we present two key use cases illustrated in Fig. 2: object placement planning and efficient object transportation.

The authors are with the STARS Lab, Institute for Aerospace Studies, University of Toronto, Toronto, Canada. {firstname.lastname}@robotics.utoronto.ca

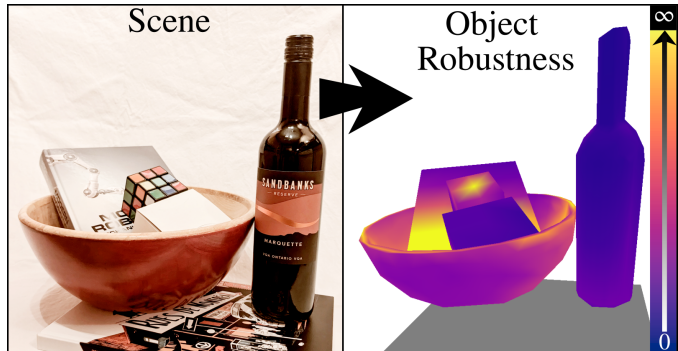


Fig. 1: Using our method, a robot can assess the robustness of objects in complex scenes (lighter colors indicates higher robustness), allowing motion planners to avoid areas close to insecure objects (e.g. the wine bottle) and object placement planners to identify stable spots (e.g. the bottom of the book).

In the first application, we show that an existing stable object placement planner [11] can produce stronger placements when using our proposed method. In the second application, we demonstrate how our method can be used to determine the acceleration that a mobile manipulator should not exceed when transporting an assembly of objects.

Due to the interplay of objects in contact, assessing the robustness of an assembly is complex and depends on the shapes, inertial parameters, frictional properties, and poses of all objects. Although heuristic methods can suffice in select applications [12, 13], a more general approach is needed to enable robots to handle diverse objects in a wide variety of scenarios. Previous efforts have resorted to computationally expensive methods, like dynamics simulations, to assess the robustness of assemblies [14, 15, 16]. In contrast, this work proposes algorithms that offer a compromise between heuristic methods and dynamics simulations, producing an accurate solution that can be used on any rigid object assembly.

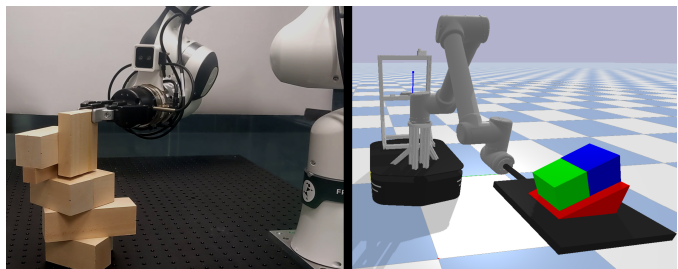


Fig. 2: Two key applications of our method: object placement planning [11] (left) and efficient transportation [1] (right).

In Sec. II, we highlight prior work on friction modeling, contact force resolution, and assembly stability assessment. The optimization problem used to compute contact forces is detailed in Sec. IV, and our proposed method for assessing the robustness of an assembly is presented in Sec. V. In Sec. VI, we highlight two key applications of our method: robust placement planning and efficient object transportation. Simulation experiments are presented in Sec. VII to demonstrate the effectiveness of the algorithms proposed in this work when combined with the placement planner from [11]. Finally, an outlook on the assumptions, advantages, and limitations of our work is provided in Sec. VIII.

II. RELATED WORK

A. Rigid Objects in Frictional Contact

Assuming that discrete contact points constitute the interface between two objects, the onset of slipping — which leads to instability — is governed by local forces at discrete contact points. For rigid objects in the elastic regime, [17] and [18] conclude that local forces at contact points on an interface between two objects are cumulative. They also show that the object deformation under load is such that the total potential energy of the system is minimized. Furthermore, results from [19] indicate that, although the local stress at contact points can be momentarily released, all contact points are maximally stressed at the onset of bulk slipping. In [20], friction is described not as a material characteristic but as a systems response that is conditioned, in part, by (i) asperities in the contact surface (e.g. ploughing), (ii) adhesion between surfaces (e.g. chemical bonding), and (iii) lubrication of the contact surface (allowing a layer of atoms to slide relative to a deeper layer). Although friction depends on factors including contact time and temperature, experiments in [21] suggest that the tangential force required to trigger slipping is reasonably well approximated by the Coulomb friction model [22] for rigid objects in the elastic regime. Our proposed algorithm makes use of the findings from [18] and [19] to model force interactions for objects with multiple contact points. Also, we base our approach on the Coulomb friction model to make it practical in common robot applications.

B. Assembly Contact Force Resolution

For an assembly to be stable, all objects must be in static force equilibrium; and enforcing this condition necessitates computing forces at the contact points. However, [23] highlights that the equilibrium condition is, in general, insufficient to guarantee stability due to indeterminacies in the contact forces. Furthermore, [24] indicates that since the deformation of an object (assumed to be rigid) is much smaller than the uncertainty in the object’s shape, the location of contact points is effectively indeterminate in practice. In this work, we select contact points optimistically and avoid static indeterminacies by relaxing the assumption that objects are perfectly rigid, an approach that is coherent with the principle of virtual work [18]. The non-linear optimization problem we use to determine

contact forces is also central to methods used in the computer-aided design of rigid structures [25, 26, 27], and is equivalent to the solution obtained with finite-element methods [28].

Rigid-body dynamics for multi-object simulations is reviewed in [29, 30], and a survey of techniques and challenges related to grasping and fixturing is presented in [5].

C. Stability Assessment

Assessing the stability of objects in contact is useful in a breadth of applications like grasp planning [3, 4, 5, 9], automated fixturing [31], object placement planning [6, 7], computer-aided design [25, 26], object transportation [1, 2]. While some methods focus on a single object (e.g. planning how to grasp or fixture a given object), the algorithm proposed in this work can be used to assess the stability of a multi-object assembly and compute its robustness to external forces.

Our approach relies on a graph representation of the assembly, similar to the one used in [32, 33] to plan disassembly sequences. The graph representation in [34] uses edges to represent the set of forces that an object can exert onto another without making it move. However, since the set of forces that object A can exert onto object B is not equal to the set of forces that B can exert onto A , [34] is limited to assemblies that can be described with directed acyclic graphs (i.e. without loops). In contrast, the graph used in our work makes our proposed algorithm applicable to any assembly of rigid objects.

The assembly robustness criterion proposed in [35] is defined as an optimization problem in which the magnitude of a given external wrench is maximized. While [35] tackles the computation of contact forces and robustness assessment in a single optimization problem, our proposed approach decouples the two such that performing the latter does not involve solving an expensive optimization problem for each external wrench query. Furthermore, [35] depends on a scaling factor to combine forces and torques into a single scalar value. In contrast, our approach based on applying forces at surface points does not require any such parameter.

Our previous work, in [11], proposes an object placement planning algorithm that can determine stable poses faster than other methods in varied rigid object scenes. In contrast to the traditional approach that samples and rejects poses, [11] selects contact points in the scene based on an approximative robustness criterion, and determine a pose that solicits the selected contact points. Compared to the heuristic used in [11], the method defined in this work assesses the assembly robustness more accurately, albeit at a higher computational cost. Upgrading [11] with our robustness criterion can improve the stability of the placement poses found and reduce the planning time when dealing with complex scenes. Furthermore, while [11] only considered the capacity of an object to *withstand* external forces, this work proposes to also consider how external forces might *improve* the overall assembly robustness.

III. NOTATION

In this work, rigid transformations are denoted using the RIGID notation convention [36] where ${}^c p_a$ is the position vector of $\{a\}$ with respect to $\{b\}$ as expressed in coordinate

system $\{c\}$, and ${}^b\mathbf{R}_a$ is the rotation matrix expressing the orientation of $\{a\}$ with respect to $\{b\}$. As defined in the RIGID convention, ${}^b\mathbf{p}_a \equiv {}_b\mathbf{p}_a$ for a more succinct notation. We denote a unit-length vector \mathbf{v} as $\hat{\mathbf{v}}$, the skew-symmetric operator as $[\mathbf{u}]_{\times} \mathbf{v} = \mathbf{u} \times \mathbf{v}$, and a $n \times n$ identity matrix as $\mathbf{1}_{n \times n}$. In this work, $\mathbf{v}_t \in \mathcal{S}^1$ and $\mathbf{v}_n \in \mathbb{R}$ respectively denote the tangential and normal components of \mathbf{v} where \mathcal{S}^1 is a unit circle in \mathbb{R}^2 .

IV. COMPUTING CONTACT FORCES

At the core of the robustness assessment problem lies the determination of forces exerted between objects in the assembly. Expressed as an optimization problem, finding values for the contact point forces in an assembly can yield no solutions, in which case the assembly is guaranteed to be unstable [37]. Otherwise, a feasible set of contact forces stabilizing the assembly can be found, with no guarantee that it represents the system of forces truly experienced by the assembly since the true contact point location is indeterminate in practice [24]. Choosing contact points amongst the exterior vertices of an interface between two contacting objects is convenient when enforcing body impenetrability [38] and when considering contact dynamics at the interface area [39]. This vertex-based contact point selection scheme, which is used in this work, leads to an optimistic robustness assessment since frictional forces are best positioned to counteract a torque about the interface normal.

A. Equilibrium Constraints

A necessary but insufficient condition for assembly stability [23] is that all objects must be in a static equilibrium, which is achieved when the sum of all forces and torques acting on the object is zero. A contact force \mathbf{f} at a contact point can be decomposed into a frictional component \mathbf{f}_t and a normal component \mathbf{f}_n , with the frictional component further decomposed into two orthogonal components \mathbf{f}_u and \mathbf{f}_v . A local reference frame can be defined as $\mathcal{F}_i = [\hat{\mathbf{u}} \ \hat{\mathbf{v}} \ \hat{\mathbf{n}}]$, where $\hat{\mathbf{u}}$, $\hat{\mathbf{v}}$, and $\hat{\mathbf{n}}$ are the unit vectors of the local frame with the inward surface normal given by $\hat{\mathbf{n}}$. The contact force at the contact point can be expressed as

$$\mathbf{f} = \mathbf{f}_t + \mathbf{f}_n = [\mathbf{f}_u \ \mathbf{f}_v \ \mathbf{f}_n]^T \quad (1)$$

in \mathcal{F}_i , where $\mathbf{f}_t = [\mathbf{f}_u \ \mathbf{f}_v]^T \in \mathcal{S}^1$ is the tangential force and \mathbf{f}_n is the normal force. The contact force can be expressed in the global (i.e. world, inertial) frame \mathcal{F}_w as

$${}^w\mathbf{f}_i = {}^w\mathbf{R}_i \mathbf{f} \quad (2)$$

where ${}^w\mathbf{R}_i$ is the rotation matrix expressing the orientation of \mathcal{F}_i with respect to \mathcal{F}_w . The wrench exerted by ${}^w\mathbf{f}_i$ on the object, and expressed in \mathcal{F}_w , is

$${}^w\mathbf{w}_i = \underbrace{\begin{bmatrix} \mathbf{1}_{3 \times 3} \\ [{}^w\mathbf{p}_i]_{\times} \end{bmatrix}}_{\mathbf{A}_i} {}^w\mathbf{f}_i = \underbrace{\begin{bmatrix} \mathbf{1}_{3 \times 3} \\ [{}^w\mathbf{p}_i]_{\times} \end{bmatrix}}_{\mathbf{B}_i} {}^w\mathbf{R}_i \begin{bmatrix} \mathbf{f}_u \\ \mathbf{f}_v \\ \mathbf{f}_n \end{bmatrix} \quad (3)$$

where ${}^w\mathbf{p}_i$ is the position of the i -th contact point relative to \mathcal{F}_w . For an object with N contact points, the sum of all wrenches exerted on the object by contact forces is given by

$$\sum_i^N {}^w\mathbf{w}_i = [\mathbf{B}_1 \ \dots \ \mathbf{B}_N] [\mathbf{f}_1^T \ \dots \ \mathbf{f}_N^T]^T \quad (4)$$

such that the equilibrium condition is defined as

$$[\mathbf{B}_1 \ \dots \ \mathbf{B}_N] [\mathbf{f}_1^T \ \dots \ \mathbf{f}_N^T]^T + {}^w\mathbf{w}_g = \mathbf{0} \quad (5)$$

where ${}^w\mathbf{w}_g$ is the wrench due to inertial forces acting at the centre of mass ${}^w\mathbf{p}_c$. In constant velocity or at rest,

$${}^w\mathbf{w}_g = m [\mathbf{1}_{3 \times 3} \quad -[{}^w\mathbf{p}_c]_{\times}]^T {}^w\mathbf{a}_g \quad (6)$$

where m is the object mass and ${}^w\mathbf{a}_g$ is gravity.

B. Friction Magnitude Constraints

The Coulomb friction model [22, 24] states that, for a contact point to avoid slipping,

$$\|\mathbf{f}_t\| \leq \mu \|\mathbf{f}_n\| \quad (7)$$

where $\mu \in \mathbb{R}_+$ is the coefficient of friction, \mathbf{f}_n is the normal force, and \mathbf{f}_t is the tangential force at the contact point, as shown in Fig. 3. Hence, in \mathcal{F}_i , the friction force must lie within a circle whose radius is $\mu \|\mathbf{f}_n\|$. The inequality in (7) can be rewritten as the equality

$$c = \mu \|\mathbf{f}_n\| - \|\mathbf{f}_t\| \quad (8)$$

where $c \in \mathbb{R}_+$ is the *contact condition*, that can be interpreted as expressing how far a contact point is from slipping.

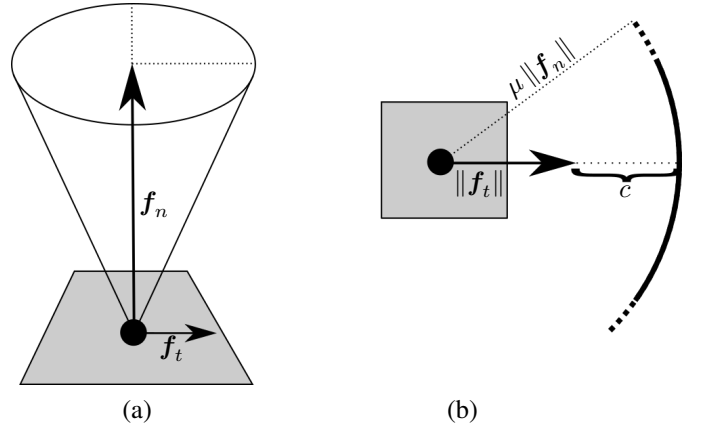


Fig. 3: (a) Coulomb friction cone with inward normal \mathbf{f}_n and tangential \mathbf{f}_t . (b) Contact condition c at the contact point.

The Coulomb circle is commonly approximated [23, 40] with an inscribed polygon, such as a square or an octagon, as shown in Fig. 4. While an inscribed square covers only about 65% of the Coulomb circle, an inscribed octagon covers about 90%. In any case, the inequality

$$\mathbf{C} [\mathbf{f}_u \ \mathbf{f}_v \ \mathbf{f}_n]^T \leq \mathbf{0}_{N \times 1} \quad (9)$$

where \mathbf{C} is a $N \times 3$ matrix whose k -th row is given by

$$\mathbf{C}[k, 1:3] = [\cos \frac{2\pi k}{N} \quad \sin \frac{2\pi k}{N} \quad -\mu \cos \frac{\pi}{N}] \quad (10)$$

enforces the friction force to lie within an inscribed N -sided regular polygon, as shown in Fig. 4.

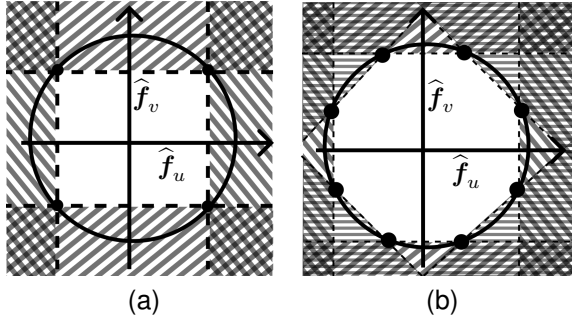


Fig. 4: Friction circle linearization with (a) $N = 4$ and (b) $N = 8$ by defining N half-plane constraints per contact point.

C. Friction Direction Constraints

With a *virtual displacement* being an infinitesimal potential displacement [3, 35], a rigid body virtual displacement can be defined as a small rotation followed by a small translation. In turn, a small rotation can be expressed as an *axis-angle* pair $(\hat{\omega}, \theta)$ where $\hat{\omega}$ is the unit-length axis about which the rotation of amplitude $\theta \approx 0$ is performed. A rotation matrix can be obtained from the axis-angle representation through the use of Rodrigues' formula

$$R = \mathbf{1}_{3 \times 3} + \sin(\theta) [\hat{\omega}]_{\times} + (1 - \cos(\theta)) [\hat{\omega}]_{\times}^2 \quad (11)$$

that can be approximated with

$$R \approx \mathbf{1}_{3 \times 3} + \theta [\hat{\omega}]_{\times} = \mathbf{1}_{3 \times 3} + [\theta \hat{\omega}]_{\times} \quad (12)$$

since $\sin(\theta) \approx \theta$ and $(1 - \cos(\theta)) \approx 0$ when $\theta \approx 0$. Hence, the displacement of a contact point can be expressed as

$${}^w \mathbf{d} = \Delta \mathbf{p} + [\theta \hat{\omega}]_{\times} {}^w \mathbf{p}_i \quad (13)$$

$$= \underbrace{[\mathbf{1}_{3 \times 3} \quad -[{}^w \mathbf{p}_i]_{\times}]}_{(\mathbf{A}^i)^{\top}} \underbrace{[\Delta \mathbf{p}^{\top} \quad \omega^{\top}]}_{{}^w \boldsymbol{\nu}_j}^{\top} \quad (14)$$

where $\Delta \mathbf{p}$ and $\omega = \theta \hat{\omega}$ are the linear displacement and rotational displacements respectively. The virtual motion twist of the j -th rigid body on which the contact point is located is denoted by ${}^w \boldsymbol{\nu}_j$. Interestingly, the matrix relating the rigid-body motion to the displacement of the contact point in (14) is the transpose of \mathbf{A}^i , which relates the local contact force to the global wrench in (3).

The virtual displacement at a contact point can be expressed in the local frame \mathcal{F}_i with

$${}^i \mathbf{d} = [d_u \quad d_v \quad d_n]^{\top} = {}_i \mathbf{R}_w {}^w \mathbf{d} \quad (15)$$

where the tangential components of the virtual displacement are constrained to be very small with $|d_u|, |d_v| \leq 10^{-3}$ while the normal component is constrained with $-10^{-3} \leq d_n \leq 10^{-5}$ to more strongly restrict interpenetration. Since friction must locally oppose virtual displacement [3, 35], the friction force at a contact point must satisfy

$${}^i \mathbf{f}_t = -\kappa_i {}^i \mathbf{d}_t \quad (16)$$

where ${}^i \mathbf{d}_t = [d_u \quad d_v]^{\top} \in \mathcal{S}^1$ and $\kappa_i \in \mathbb{R}_+$ relates the magnitude of the friction force to the magnitude of the

virtual displacement, akin to a spring constant. According to [26], enforcing the friction direction constraint in (16) at all contact points implicitly enforces the consistency of kinematic constraints [39] between objects and restricts ${}^w \boldsymbol{\nu}_j$ to feasible motions.

D. Unilaterality Constraints

Contact forces acting on a rigid body must be compressive [25], which can be enforced with

$$\mathbf{f}_n \geq 0 \quad (17)$$

assuming that $\hat{\mathbf{n}}$, along which \mathbf{f}_n is directed, is the inward normal of the object surface at the contact point.

E. Normal Force and Displacement Complementarity

At a point on the interface between two objects, either the normal force or the normal displacement must be zero, since no force can be transmitted when there is a gap between the objects. This *complementarity* between normal force and normal displacement gives rise to $\mathbf{f}_n \mathbf{d}_n = 0$ that can be softened with

$$\mathbf{f}_n (\mathbf{d}_n - \epsilon) = 0 \quad (18)$$

through the use of a small positive slack variable $\epsilon \leq 10^{-5}$ that allows for some interpenetration [3, 35].

F. Objective Function

The assumption that objects within an assembly are perfectly rigid can lead to statically indeterminate problems, which can only be solved by departing from the assumption and considering the potential energy due to small deformations in the object [18]. For stiff materials, the real contact area is much smaller than the apparent contact area [21] and the applied force needed to slightly deform the contacting asperities is governed by Young's modulus κ with $\|\mathbf{f}\| = \kappa x$ where x is the magnitude of the deformation. The energy stored through the deformation is given by

$$U = \int \|\mathbf{f}\| dx = \frac{\kappa x^2}{2} = \frac{\|\mathbf{f}\|^2}{2\kappa} \quad (19)$$

and increases quadratically with the magnitude of the applied force. The *principle of virtual work* dictates that a system will go through states that cumulatively minimize the system's energy — the path of least action [18]. With the energy in (19) being proportional to the square of the applied force, the principle of virtual work dictates that the sum of squared contact forces should be minimized.

G. Optimization Problem

With J being the set of objects, I being the set of all contact points across all objects, and K_j being the set of contact points

on object $j \in J$, the complete formulation of the optimization problem for computing the contact forces in an assembly is

$$\min_{(\mathbf{f}_i, {}_w\boldsymbol{\nu}_j, \kappa_i) \forall i, j} \sum_i^N \|\mathbf{f}_i\|^2 \quad (20)$$

subject to

$$\sum_k^{K_j} \mathbf{B}_k \mathbf{f}_k + {}_w\mathbf{w}_{g_j} = \mathbf{0} \quad \forall j \in J \quad (21)$$

$$\mathbf{C}_i \mathbf{f}_i \leq \mathbf{0} \quad \forall i \in I \quad (22)$$

$${}^i \mathbf{d}_k = \mathbf{B}_k^T {}_w\boldsymbol{\nu}_j \quad \forall k \in K_j, \forall j \in J \quad (23)$$

$${}^i \mathbf{f}_t = -\kappa_i {}^i \mathbf{d}_t \quad \forall i \in I \quad (24)$$

$${}^i \mathbf{f}_n \geq \mathbf{0}, \kappa_i \geq 0 \quad \forall i \in I \quad (25)$$

$${}^i \mathbf{f}_n ({}^i \mathbf{d}_n + \epsilon) = \mathbf{0} \quad \forall i \in I \quad (26)$$

representing a quadratic program with non-linear constraints that can be solved using interior-point methods [41].

V. COMPUTING THE STATIC ROBUSTNESS

In evaluating the forceful perturbations that a static assembly can withstand, two phenomena are considered: slipping and toppling. Slipping occurs when contact conditions become zero, while toppling occurs when an external force overcomes the torque exerted by the weight of the assembly. A key strategy in our approach is to deal with slipping and toppling separately, as they are fundamentally different phenomena, and then combine both results at the end. The combination, termed *static robustness*, is given as the minimum between the force causing slipping and the one causing toppling.

Definition 1: The *static robustness* is the amount of force that can be applied in a given direction on a given point before slipping or toppling occurs in a static assembly. With \mathbb{R} being the set of real numbers and \mathbb{S}^2 being the unit sphere, static robustness is defined as

$$\text{SR} : \mathbb{R}^3 \times \mathbb{S}^2 \rightarrow \mathbb{R}_+ \quad (27)$$

which maps a pair $({}_w\mathbf{p}_i \in \mathbb{R}^3, {}_w\hat{\mathbf{e}}_i \in \mathbb{S}^2)$ to the maximum force magnitude $\text{SR} \in \mathbb{R}_+$ that can be exerted on point ${}_w\mathbf{p}_i$ in the direction ${}_w\hat{\mathbf{e}}_i$ before the onset of motion.

In turn, this work also proposes a method to determine how applying an external force can improve or reduce the static robustness of the assembly.

Definition 2: The *static robustness improvement* is the difference in static robustness that results from applying an external force on a given point in a given direction. Static robustness improvement is defined as

$$\text{SRI} : \mathbb{R}^3 \times \mathbb{S}^2 \rightarrow \mathbb{R} \quad (28)$$

which maps a pair $({}_w\mathbf{p}_i \in \mathbb{R}^3, {}_w\hat{\mathbf{e}}_i \in \mathbb{S}^2)$ to the difference $\text{SRI} \in \mathbb{R}$ in static robustness that results from applying an external force on point ${}_w\mathbf{p}_i$ in the direction ${}_w\hat{\mathbf{e}}_i$.

Although any point in \mathbb{R}^3 can be considered, it makes sense to restrict ourselves to points on the surface of the objects where contact can occur. Assuming that $0 \leq \mu \leq 1$ (which is the case for most materials combinations), at all contact points $\|\mathbf{f}_n\| \geq \|\mathbf{f}_t\|$ when objects are stable. Likewise, any

direction in \mathbb{S}^2 can be considered, however external force is likely to be applied normal to the surface such as to maximize the contact conditions. Hence, computing the static robustness for points on the surface of the objects and directions normal to the surface is a natural choice.

A. Contact Interface Graph

An arbitrary structure of rigid objects can be described with a *contact interface graph* (CIG) in which each node represents an object in the assembly and each edge represents a contact interface [42] between two objects, as shown in Fig. 5.

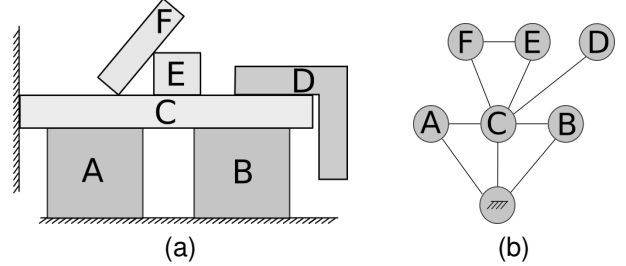


Fig. 5: (a) A structure composed of six non-fixed objects and two fixed objects (i.e. floor and wall). (b) The contact interface graph of the structure with the fixed nodes at the bottom.

The information contained in the CIG can be stored as a list of interfaces, each defined by the two objects it connects, the locations of the contact points on the interface, and the forces at the contact points. To simplify the graph, nodes representing fixed objects (e.g. a floor, a wall) can be merged into a single node marked as being *fixed*. The resulting graph is guaranteed to be connected such that a path exists from any node to the fixed node, and a *support relations graph* [43] can easily be derived from the CIG. A *directional force graph* [32] describing the forces required to extract an object from a fixtured assembly can also be derived from the CIG. Similar to the approach taken in [34], the CIG can be iteratively simplified through edge contraction to yield an equivalent CIG. However, in contrast to [34], edges in the CIG are undirected and the contraction operations are commutative, such that the presence of cycles in the graph is not a problem.

When a force is exerted on a node, all interfaces lying on simple paths between the node and the fixed node will incur additional stress since (20) dictates that stress should be spread as much as possible. Deformations occur when an object is constrained by a force and the environment (e.g. an object falling down under gravitational force will deform only when hitting the ground). Hence, objects not lying on the aforementioned paths are not further constrained by the applied force and will not incur additional stress.

B. Robustness to Slipping

Let the contact force \mathbf{f} at a given contact point be expressed in a local frame as $\mathbf{f} = [\mathbf{f}_u \ \mathbf{f}_v \ \mathbf{f}_n]^T$ where $\mathbf{f}_t = [\mathbf{f}_u \ \mathbf{f}_v]^T \in \mathcal{S}^1$ is the tangential force and \mathbf{f}_n is the normal force, as pictured in Fig. 3. Also, let an external force applied at the contact point be expressed in the local frame

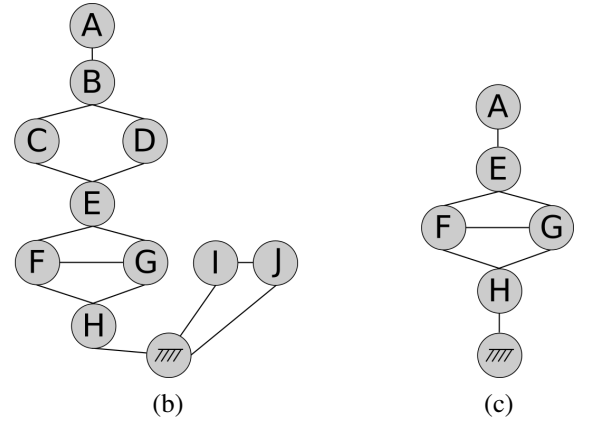
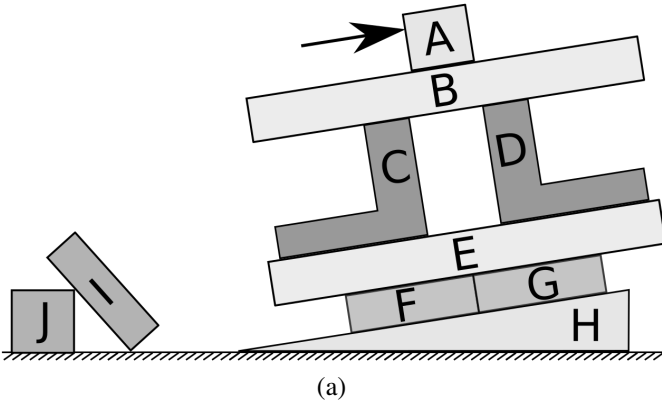


Fig. 6: (a) A structure upon which a force is exerted and its corresponding CIG (b). (c) The CIG following simplification where nodes I and J were trimmed and edges between A and E were contracted with $AE = \min \{AB, \min \{BC, CE\} + \min \{BD, DE\}\}$. The slipping robustness of A to the external force is given by the maximum flow in (c) where the capacity of each edge is the slipping robustness of the corresponding interface.

as $\mathbf{e} = s\hat{\mathbf{e}} = [e_u \ e_v \ e_n]^\top$ where $s \in \mathbb{R}_+$ is the magnitude of the external force and $\hat{\mathbf{e}} \in \mathbb{S}^2$ is its direction. The *contact condition* of the point can be expressed as

$$c(s) = \mu \|\mathbf{f}_n + s\hat{\mathbf{e}}_n\| - \|\mathbf{f}_t + s\hat{\mathbf{e}}_t\| \quad (29)$$

that equals zero when

$$\mu \|\mathbf{f}_n + s\hat{\mathbf{e}}_n\| = \|\mathbf{f}_t + s\hat{\mathbf{e}}_t\|, \quad (30)$$

at which point the contact point is on the verge of slipping. Equation (30) is quadratic in s with solutions given by

$$s_m = \frac{[\mathbf{f}_u \ \mathbf{f}_v \ -\mu^2 \mathbf{f}_n] \hat{\mathbf{e}} - n}{d}, \quad s_p = s_m + \frac{2n}{d} \quad (31)$$

where

$$n = \left(\mu^2 (\hat{\mathbf{e}}_n \mathbf{f}_u - \hat{\mathbf{e}}_u \mathbf{f}_n)^2 + \mu^2 (\hat{\mathbf{e}}_n \mathbf{f}_v - \hat{\mathbf{e}}_v \mathbf{f}_n)^2 - (\hat{\mathbf{e}}_v \mathbf{f}_u - \hat{\mathbf{e}}_u \mathbf{f}_v)^2 \right)^{\frac{1}{2}} \quad (32)$$

$$d = \mu^2 \|\hat{\mathbf{e}}_n\|^2 - \|\hat{\mathbf{e}}_t\|^2 \quad (33)$$

are used to simplify the notation. The solution in (31) can be shown to be equivalent to the geometric problem of finding intersection points between an external force vector and the friction cone at a contact point, as derived in [11]. The curvature of the equation in (30) is given by d such that

$$s_m = \frac{\|\mathbf{f}_t\|^2 - \mu^2 \|\mathbf{f}_n\|^2}{2(\mu^2 \|\hat{\mathbf{e}}_n\| \|\mathbf{f}_n\| - \hat{\mathbf{e}}_t^\top \mathbf{f}_t)} \quad \text{when } d = 0 \quad (34)$$

is the solution to the linear equation obtained when $\mu^2 \|\hat{\mathbf{e}}_n\|^2 = \|\hat{\mathbf{e}}_t\|^2$. Assuming that $c(0) \geq 0$ (i.e. the assembly is stable when no external force is applied), four situations can be considered depending on the sign of d and on the sign of $\partial c / \partial s$ at $s = 0$. The four situations are shown in Fig. 7, with inset figures representing the friction cone with contact and external force directions at the contact point. When positive, the solution s_m represents the maximum amount of force that can be exerted on the contact point in the direction $\hat{\mathbf{e}}$ before slipping occurs (s_p could equivalently be used for

this purpose). When $s_m < 0$, an infinite amount of force can be exerted in the direction $\hat{\mathbf{e}}$ without slip occurring, such that

$$\text{SR}_{\text{slip}}(w\mathbf{p}_i, w\hat{\mathbf{e}}_i) = \begin{cases} s_m & \text{if } s_m \geq 0 \\ \infty & \text{if } s_m < 0 \end{cases} \quad (35)$$

where $\text{SR}_{\text{slip}}(w\mathbf{p}_i, w\hat{\mathbf{e}}_i)$ is the robustness to slipping when $w\hat{\mathbf{e}}_i$ is exerted on point $w\mathbf{p}_i$.

The situation depicted in Fig. 7a represents the case where any non-zero external force (starting from $s = 0$) will decrease the contact condition. In Fig. 7b, increasing the magnitude of the external force will first improve the contact condition by bringing the sum of forces closer to the axis of the friction cone, but increasing it further will monotonically decrease the contact condition. In Fig. 7c, the external force is inside the friction cone at the contact point, and any amount of force will improve the contact condition. In Fig. 7d, the external force is inside the cone that is opposed to the friction cone and increasing the magnitude of the external force will decrease the contact condition until it reaches zero and break.

C. Slipping Robustness Improvement

As shown in Fig. 7b and Fig. 7c, exerting force on a contact point can improve the contact condition. However, in the situation depicted in Fig. 7b, exceeding a certain amount of force will decrease the contact condition until slipping occurs. When planning the placement of an object, it can be beneficial to consider how applying an external force can improve or reduce the robustness of the assembly.

Taking the derivative of the contact condition in (29) with respect to the magnitude of the external force yields

$$\frac{\partial c}{\partial s} = \mu \hat{\mathbf{e}}_n - \frac{\hat{\mathbf{e}}_u (s\hat{\mathbf{e}}_u + \mathbf{f}_u) + \hat{\mathbf{e}}_v (s\hat{\mathbf{e}}_v + \mathbf{f}_v)}{\sqrt{(s\hat{\mathbf{e}}_u + \mathbf{f}_u)^2 + (s\hat{\mathbf{e}}_v + \mathbf{f}_v)^2}} \quad (36)$$

$$= \mu \hat{\mathbf{e}}_n - \frac{\hat{\mathbf{e}}_t^\top (\mathbf{f}_t + s\hat{\mathbf{e}}_t)}{\|\mathbf{f}_t + s\hat{\mathbf{e}}_t\|} \quad (37)$$

where the rightmost term can be interpreted as the projection of the tangential external force vector onto the total tangential

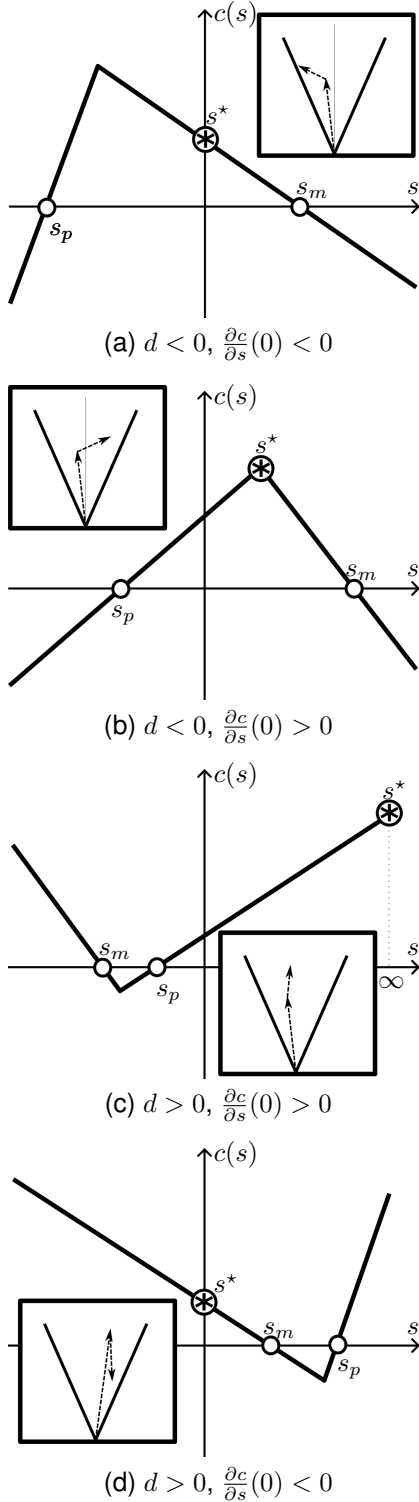


Fig. 7: The contact condition as a function of the external force magnitude. The roots of $c(s)$ are s_m and s_p while s^* is the magnitude that should be exerted to maximize c . Inset figures represent the friction cone with the external force starting at the tip of the contact force.

force vector. From (37), the contact condition will be improved if the projection of the external force onto the contact point normal is above a threshold value determined by the coefficient of friction. In appendix A, the expression in (37) is used to determine the magnitude of the external force that will improve the contact condition the most.

D. Slipping Robustness of an Assembly

In general, an object will be in contact with several other objects through contact points that have different maximal frictional force (i.e. traction limit). Assuming that contact points obey the laws of linear elasticity, the stress incurred at each contact point is cumulated to produce the total frictional force [18, 21]. Locally, the stress on an asperity can be momentarily released with another asperity taking over the load, but the gross effect is that the total frictional force is the sum of the frictional forces at each contact point [19]. This is consistent with the *principle of least action*: the system will naturally minimize its energy by distributing the forces as uniformly as possible on contact points, each respecting its traction limit. Hence, we state:

Assertion 1: The slipping robustness of several contact points or interfaces acting in parallel in the CIG is given by the sum of the contact point robustnesses.

When two objects are in contact, the principle of action-reaction (i.e. Newton's third law) implies that the force acting on an interface is exerted onto both objects (with opposite directions). Hence, the maximum force that can be exerted at the interface by either object is given by the minimum traction of the two objects. In other words, in regards to slipping, a chain of objects will only be as strong as the weakest interface along the chain. This leads to the following assertion:

Assertion 2: The slipping robustness of several contact points or interfaces acting in series in the CIG is given by the minimum of the robustnesses along the series.

Given assertion 1 and assertion 2, the problem of determining the slipping robustness of a target object in an assembly can be cast as a maximum flow problem and solved with standard algorithms [44]. This is accomplished by defining a force flow network $G = (\mathcal{V}, \mathcal{E})$ where \mathcal{V} is the set of nodes in the CIG and \mathcal{E} is the set of edges. In G , the source node is set to the target object while the fixed object is the sink. Each edge in the network is given a capacity equal to the sum of the corresponding interface contact point robustnesses, as computed with (35). The slipping robustness of the target object is then given by the maximum flow in the network. This type of network has been used in [33, 32] to study how clusters of parts in fixtured assemblies can be disassembled.

Since the time complexity of the algorithm used to solve the maximum flow problem is $O(|\mathcal{V}|^2|\mathcal{E}|)$, the computation time can be reduced by simplifying the CIG prior to the initialization of the force flow network. First, nodes not lying on simple paths between the target and fixed objects can be removed from the graph. Also, similar to the approach in [34], edges can be iteratively contracted with the following rules:

- Given assertion 1, two parallel edges can be combined into a single equivalent edge with a capacity equal to the sum of the capacities of the two edges.

- Given assertion 2, two edges in series can be combined into a single equivalent edge with a capacity equal to the minimum of the capacities of the two edges.

In general, however, it might not be possible to simplify the CIG to a single edge, and the maximum flow problem will have to be solved on the simplified graph, as shown in Fig. 6.

Given the aforementioned assertions, the global improvement in an assembly's robustness to slipping due to an external force is given as the summation of (37) computed for all interfaces lying on simple paths connecting the external force to the fixed object in the CIG.

E. Robustness to Toppling

In some cases, an assembly with very good contact conditions will still be vulnerable to small external forces that would cause it to topple. In the following, the contact conditions are assumed to be ideal (i.e. infinite friction) so as to focus on the toppling phenomenon. In such cases, the maximal sustainable force is the one that would trigger a rotation of the object around a pivot axis, with the edges of the contact point convex hull representing potential toppling axes. In general, kinematic constraints exerted by the environment will prevent the object from rotating about some axes. Assuming ideal contact conditions, frictional forces can also prevent the object from rotating about some axes. In other words, the feasible motions that the object can experience are those for which the infinitesimal displacement at all contact point is a detachment, as illustrated in Fig. 8.

For assemblies comprising multiple objects, it is possible that a subset of the objects topple together while the others remain stable. For instance, in Fig. 5, objects C, D, E, F could topple together to the right while objects A and B remain stationary. Hence, it is necessary to consider all sub-sets of objects in contact to compute the toppling robustness of the assembly. The object sub-sets are given by the set of connected sub-graphs in the CIG not containing any fixed object.

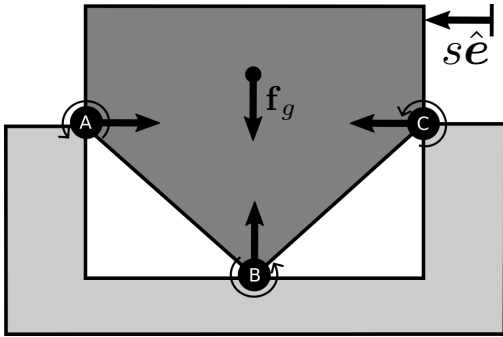


Fig. 8: Determining toppling axes. Toppling about B or C is impossible because the force at A and B, respectively, would oppose the moment exerted by $s\hat{e}$. However, toppling about A is possible because no contact force would oppose the motion.

Algorithm. For every connected sub-graph $g_i \in \mathcal{G}$, execute the following steps.

Step 1: Consider all objects in g_i to form a single agglomerated object (a super-object). Consider the contact points between

the super-object and other objects in the CIG.

Step 2: With the position of the i -th contact point being ${}^w p_i$, and with the orientation of a frame ${}^w R_i$ at the contact point being such that the z -axis is pointing into the super-object, define the grasp matrix \mathbf{G} as

$$\mathbf{G}_i = \begin{bmatrix} {}^w R_i & -{}^w R_i [1:3, 1:2] \\ [{}^w p_i]_{\times} {}^w R_i & ([{}^w p_i]_{\times} {}^w R_i) [1:3, 1:2] \end{bmatrix} \quad (38)$$

$$\mathbf{G} = [\mathbf{G}_1 \ \cdots \ \mathbf{G}_i \ \cdots \ \mathbf{G}_I] \quad (39)$$

where each contact is modelled as a *hard-finger* [42], I is the number of contact points, and $\mathbf{X}_{[1:3, 1:2]}$ is the submatrix built from the elements in the first three rows and first two columns of \mathbf{X} . The columns of \mathbf{G} are the constraining wrenches exerted by the contact points. If $\text{rank}(\mathbf{G}) < 6$, then the super-object is not form-closed [45] and a motion is possible. Otherwise, finding a solution to the linear program

$$\min_{\mathbf{x}} \sum_i x_i \quad \text{s.t.} \quad \mathbf{G}\mathbf{x} = \mathbf{0} \quad \text{and} \quad x_i \geq 1 \quad (40)$$

determines that the super-object is form-closed, in which case it cannot topple about any axis and the next super-object can be immediately considered [39].

Step 3: Compute the convex hull over the contact points between the super-object and the environment, and define two potential axes for each edge of the convex hull with

$$\mathbf{a}_i = {}^{w} p_{k_{s_i}}^{k_{t_i}} \quad \forall (k_{s_i}, k_{t_i}) \in \mathcal{K} \quad (41)$$

$$\mathbf{a}_{|\mathcal{K}|+i} = -\mathbf{a}_i \quad (42)$$

where k_{s_i} and k_{t_i} are the source and target points of the i -th edge of the convex hull, and \mathcal{K} is the set of convex hull edges whose cardinality is $|\mathcal{K}|$. Build the matrix of axis motion twists

$$\mathbf{M} = \begin{bmatrix} [{}^w p_{a_1}]_{\times} \hat{\mathbf{a}}_1 & \cdots & [{}^w p_{a_N}]_{\times} \hat{\mathbf{a}}_N \\ \hat{\mathbf{a}}_1 & \cdots & \hat{\mathbf{a}}_N \end{bmatrix} \quad (43)$$

in which the n -th column defines the twist of the corresponding axis, $N = 2|\mathcal{K}|$, and ${}^w p_{a_i} \equiv {}^w p_{k_{s_i}}$ to lighten the notation. Compute

$$\mathbf{V} = [\mathbf{V}_1^T \ \cdots \ \mathbf{V}_I^T]^T = \mathbf{G}^T \mathbf{M} \quad (44)$$

where $\mathbf{V}_i = \mathbf{G}_i^T \mathbf{M}$ is a $5 \times N$ matrix in which the (j, k) -th element is the contact point displacement about the k -th axis due to the wrench in the j -th column of \mathbf{G}_i . Verify that the normal displacement of each contact point in its local frame (assuming the third row is associated with the inward normal) is detaching upon rotation about \mathbf{a}_n with

$$\mathbf{V}_i [3, n] < -\epsilon \quad \forall i \in [1, \dots, I] \quad (45)$$

where ϵ is a small positive constraint violation tolerance. The set of valid axes \mathcal{A} includes all axes for which (45) is verified. For each $\mathbf{a} \in \mathcal{A}$, execute the following two steps.

Step 4: Since the toppling motion of the super-object requires that contact points with the environment detach (except those on the rotation axis), the gravitational force acting at the centre of mass of the super-object can be considered to be the sole external force. Hence, toppling will occur when the torque exerted by the gravitational force about \mathbf{a} is overcome.

Compute the torque exerted by the gravitational force about axis \mathbf{a} with

$${}^w_a\boldsymbol{\tau}_g = \left({}^w_{k_s}\mathbf{p}_c \times \mathbf{f}_g \right) \cdot \hat{\mathbf{a}} \quad (46)$$

where ${}^w_{k_s}\mathbf{p}_c$ is the position of the super-object centre of mass relative to the source point of \mathbf{a} , and \mathbf{f}_g is the gravitational force acting on the super-object.

Step 5: For each point e on super-object g_i for which the toppling robustness is desired, compute the maximal force that can be exerted in direction $\hat{\mathbf{e}}$ at ${}^w\mathbf{p}_e$ before the object topples about $\hat{\mathbf{a}}$ with

$$s({}^w\mathbf{p}_e, \hat{\mathbf{e}}, \hat{\mathbf{a}}, g_i) = \left| \frac{{}^w_a\boldsymbol{\tau}_g}{\left({}^w_{k_s}\mathbf{p}_e \times \hat{\mathbf{e}} \right) \cdot \hat{\mathbf{a}}} \right| \quad (47)$$

and update the toppling robustness at e as the minimum of the robustnesses computed for each axis with

$$\text{SR}_{\text{top}}(e, \hat{\mathbf{e}}) = \min_{g_i \in \mathcal{G}} \left\{ \min_{\hat{\mathbf{a}} \in \mathcal{A}} \{s(e, \hat{\mathbf{e}}, \hat{\mathbf{a}}, g_i)\} \right\}. \quad (48)$$

F. Toppling Robustness Improvement

Consider a rigid body that is in static equilibrium and subject to a set of external forces (e.g. gravity, other objects leaning on it) in \mathcal{F} , as shown in Fig. 9. Assuming that no slipping is happening, a sufficiently large external force applied to the object will cause it to topple about some axis unless the object is kinematically constrained, as determined in § V-E. However, a well-selected external force $s\hat{\mathbf{e}}$ can also reduce the torque exerted about some of the axes, thereby improving the object's robustness to toppling.

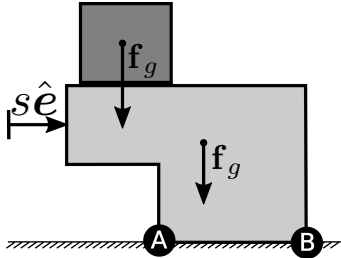


Fig. 9: Exerting a force $s\hat{\mathbf{e}}$, can help support the darker object. However, if s is too large, the light grey object will topple to the right about pivot axis B. The ideal magnitude of the external force is the one that maximizes the force required to topple the object about both axes.

With \mathcal{A} being the set of toppling axes on interfaces connecting the target object to other objects closer to the root of the CIG, let ${}^w\mathbf{p}_e$ be a point on the object where an external force $s\hat{\mathbf{e}}$ is applied (whose magnitude is s and direction $\hat{\mathbf{e}}$).

Let ${}^w_{a_i}\boldsymbol{\tau}_g$ be the torque exerted by gravity about toppling axis $a_i \in \mathcal{A}$, as defined in (46), and let

$${}^w_{a_i}\boldsymbol{\tau}_e = \left({}^w_{k_{s_i}}\mathbf{p}_e \times \hat{\mathbf{e}} \right) \cdot \hat{\mathbf{a}}_i \quad (49)$$

be the torque exerted by the unit-length external force $\hat{\mathbf{e}}$ about axis \mathbf{a}_i with ${}^w_{k_{s_i}}\mathbf{p}_e$ being the position of the external force relative to the source point of \mathbf{a}_i . With

$$\mathbf{A} = \begin{bmatrix} {}^w_{a_1}\boldsymbol{\tau}_e & \cdots & {}^w_{a_N}\boldsymbol{\tau}_e \end{bmatrix}^T \quad (50)$$

$$\mathbf{b} = \begin{bmatrix} {}^w_{a_1}\boldsymbol{\tau}_g & \cdots & {}^w_{a_N}\boldsymbol{\tau}_g \end{bmatrix}^T \quad (51)$$

$$\mathbf{x} = [s] \quad (52)$$

the external force magnitude given by

$$s^* = \underset{\mathbf{x}}{\text{argmin}} \|\mathbf{A}\mathbf{x} - \mathbf{b}\|^2 \quad (53)$$

minimizes the torque exerted about all axes in \mathcal{A} . In appendix A a closed-form solution for s^* is derived.

The derivative of the objective in (53) with respect to the magnitude of the external force [46] is given by

$$\frac{\partial}{\partial s} \|\mathbf{A}\mathbf{x} - \mathbf{b}\|^2 = 2\mathbf{A}^T\mathbf{A}\mathbf{x} - 2\mathbf{A}^T\mathbf{b} \quad (54)$$

and represents how $s\hat{\mathbf{e}}$ at ${}^w\mathbf{p}_e$ globally increases the odds of toppling. In turn,

$$2 \left(\mathbf{A}^T\mathbf{b} - \mathbf{A}^T\mathbf{A}\mathbf{x} \right) = 2 \sum_a {}^w_a\boldsymbol{\tau}_g {}^w_a\boldsymbol{\tau}_e - 2s \sum_a {}^w_a\boldsymbol{\tau}_e^2 \quad (55)$$

represents how a force directed along $\hat{\mathbf{e}}$ and exerted at ${}^w\mathbf{p}_e$ improves the object's robustness to toppling. Notice that (55) depends on s , whose value should be selected based on the expected external force magnitude. For instance, in the placement planning experiments conducted in this work, (55) was evaluated with s set to one-third of the weight of the object being placed since three contact points are required for equilibrium.

In multi-object assemblies, (55) can be computed for all interfaces lying on simple paths connecting the external force to the fixed object in the CIG, as described in § V-A, and summed to determine the global improvement in the object's robustness to toppling when the external force is applied.

VI. APPLICATIONS

A. Object Placement Planning

The problem of stably placing a given object in an existing assembly is challenging since feasible poses must (1) make contact with the environment while avoiding interpenetrations, and (2) exert forces upon all objects in the assembly while preserving the force equilibrium of the system. Consequently, a very small region of the solution space is feasible, and searching for stable placements by iterating over a discretized set of poses is inefficient and computationally expensive [11]. As proposed in [11], the static robustness of points on objects in the assembly can be used to efficiently guide the search for stable poses by sampling robust contact points and determining poses that would solicit the selected contact points. To do so, a SR *map* is computed as $\{\text{SR}(\mathbf{p}, \hat{\mathbf{n}}) \forall \mathbf{p} \in \mathcal{P}\}$, where \mathcal{P} is the set of points on the objects, and $\hat{\mathbf{n}}$ is the normal to the surface at \mathbf{p} , an example of which is shown in Fig. 1. While the approximate approach in [11] reduced computational complexity by considering only a subset of the constraints in (20)–(26) and each object in

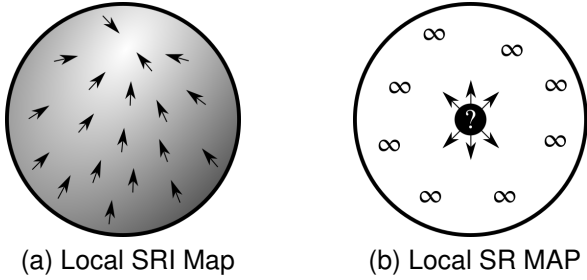


Fig. 10: The gradient of the SRI map (a) is defined even where the corresponding SR map (b) only contains infinite values, enabling the local optimization of contact point positions.

isolation, the method proposed in this work can be used to compute the exact static robustness of an assembly, albeit at a higher computational cost. Hence, our approach can be seamlessly integrated into the planner proposed in [11] to improve the reliability of the placements found.

As shown in Table I, in which each object point is coloured based on its SR/SRI value for a force exerted normal to the surface at that point, the SR map can contain areas of points with infinite robustness (coloured black). In contrast, the SRI map does not contain any infinite values, which is advantageous for object placement planning for two reasons.

First, the absence of infinite values makes contact point sampling more efficient since it offers a way to choose between points with infinite static robustness. For instance, when sampling points on the cube in Table Ia, all points on the top face have the same likelihood of being selected, irrespective of whether they are in the centre or closer to the edges. However, from § V-E, we know that exerting a force in the centre is objectively better. Since this issue is not present when sampling points based on the SRI map, the probability function proposed in [11] can be simplified to

$$w(\mathbf{p}) = \max(0, \text{SRI}(\mathbf{p}, \hat{\mathbf{n}}) - \lambda^k \text{SRI}_{\max}) \quad (56)$$

$$P(\mathbf{p}) = \frac{w(\mathbf{p})}{\sum w(\mathbf{p})} \quad \forall \mathbf{p} \in \mathcal{P} \quad (57)$$

where $\text{SRI}(\mathbf{p}, \hat{\mathbf{n}})$ is the SRI value at \mathbf{p} for a force normal to the surface, $\text{SRI}_{\max} = \max(\{\text{SRI}(\mathbf{p}, \hat{\mathbf{n}}) \mid \mathbf{p} \in \mathcal{P}\})$, k is the iteration number, and λ is the threshold decay rate — the only parameter of the probability function.

A second advantage of not having infinite values in the SRI map pertains to the possibility of using the SRI values to perform a local optimization of the object pose such as to improve the static robustness of the assembly. As pictured in Fig. 10a, a gradient of the SRI map is defined everywhere and can be used to move a contact point towards a position with higher SRI. In contrast, the gradient of the SR map is zero on patches of points with infinite robustness (where the object should probably be placed) as shown in Fig. 10b. This key advantage of the SRI map is leveraged to define a local pose optimization algorithm, described in Algorithm 1, that iteratively perturbs and aligns (IPA) a preliminary object pose to solicit points with greater SRI values. To do so, IPA first perturbs the contact point positions by moving them slightly

closer to the centre of mass of the object (step 2). Then, the K nearest neighbours of each contact point are found in the SRI map and the point with the maximal SRI value is selected (step 3). Making use of the Kabsch algorithm [47], a transformation that positions the object’s mass on points with higher SRI is determined and applied to the object pose (step 4). Since the transformation may have caused the object to penetrate or detach from the scene, the object is re-aligned to the scene in step 5. The process is repeated until the pose transformation converges or a maximum number of iterations is reached.

An example of the IPA algorithm in action from one of our placement planning experiments is shown in Fig. 11, in which the initial pose selected for the placement of a cube is marginally stable at best. Executing the IPA algorithm iteratively transforms the pose of the cube such that it rests on the flat area of the slant where the SRI values are higher.

Algorithm 1: Iterative Perturb and Align (IPA)

input : SRI map $\text{SRI}(\mathbf{p}, \hat{\mathbf{n}}) \forall \mathbf{p}$, object pose wT_o and centre of mass \mathbf{c} , perturbation magnitude M

output: Optimized object pose ${}^wT_o^+$

while wT_o not converged **do**

1. Detect contact points and penetration points
2. Perturb the object contact points \mathcal{B}

$$\mathbf{v} \leftarrow \text{diag}([1, 1, 0]) (\mathbf{c} - \sum \mathcal{B}_i / |\mathcal{B}|)$$

$$\mathcal{B}_i \leftarrow \mathcal{B}_i + M\mathbf{v} / \|\mathbf{v}\| \quad \forall \mathcal{B}_i \in \mathcal{B}$$
3. For each point in \mathcal{B} , find the scene point \mathcal{S}_i with maximal SRI amongst its K nearest neighbours
$$\mathcal{S}_i \leftarrow \text{argmax} \{ \text{SRI}(\mathbf{p}, \hat{\mathbf{n}}) \mid \mathbf{p} \in \text{KNN}(\mathcal{B}_i) \}$$
4. Align \mathcal{B} to \mathcal{S} using the Kabsch algorithm
$$\tilde{\mathcal{B}} \leftarrow \mathcal{B} - \sum \mathcal{B}_i / |\mathcal{B}|$$

$$\tilde{\mathcal{S}} \leftarrow \mathcal{S} - \sum \mathcal{S}_i / |\mathcal{S}|$$

$$\mathbf{U}, \mathbf{S}, \mathbf{V} \leftarrow \text{svd}(\tilde{\mathcal{B}}^T \tilde{\mathcal{S}})$$

$$\mathbf{R} \leftarrow \mathbf{U} \text{diag}([1, 1, \det(\mathbf{UV}^T)]) \mathbf{V}^T$$

$$\mathbf{t} \leftarrow \sum \mathcal{S}_i / |\mathcal{S}| - \mathbf{R} \sum \mathcal{B}_i / |\mathcal{B}|$$

$${}^w\mathbf{R}_o^+ \leftarrow \mathbf{R} {}^w\mathbf{R}_o$$

$${}^w\mathbf{p}_o^+ \leftarrow \mathbf{t} + {}^w\mathbf{p}_o$$
5. Align the object to the scene
 Select \mathcal{B} uniformly on the object
 Find closest \mathcal{S}_i to all $\mathcal{B}_i \in \mathcal{B}$
 Keep correspondences if $\|\mathcal{S}_i - \mathcal{B}_i\| \leq D$
 Align \mathcal{B} to \mathcal{S} using the Kabsch algorithm

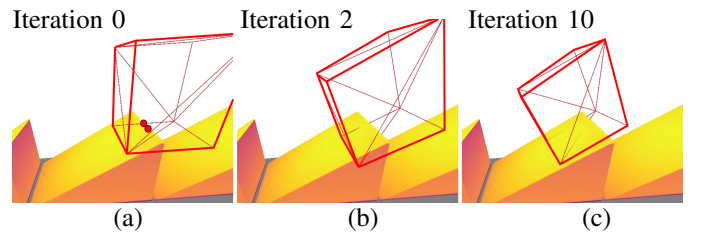


Fig. 11: The proposed IPA algorithm used to refine the placement of a cube (outlined in red with seed contact points as red dots) within the *Sawteeth* scene from our experiments. The initial pose (a) is unstable and iteratively transformed to a stable pose (b) resting on points with higher SRI values (c).

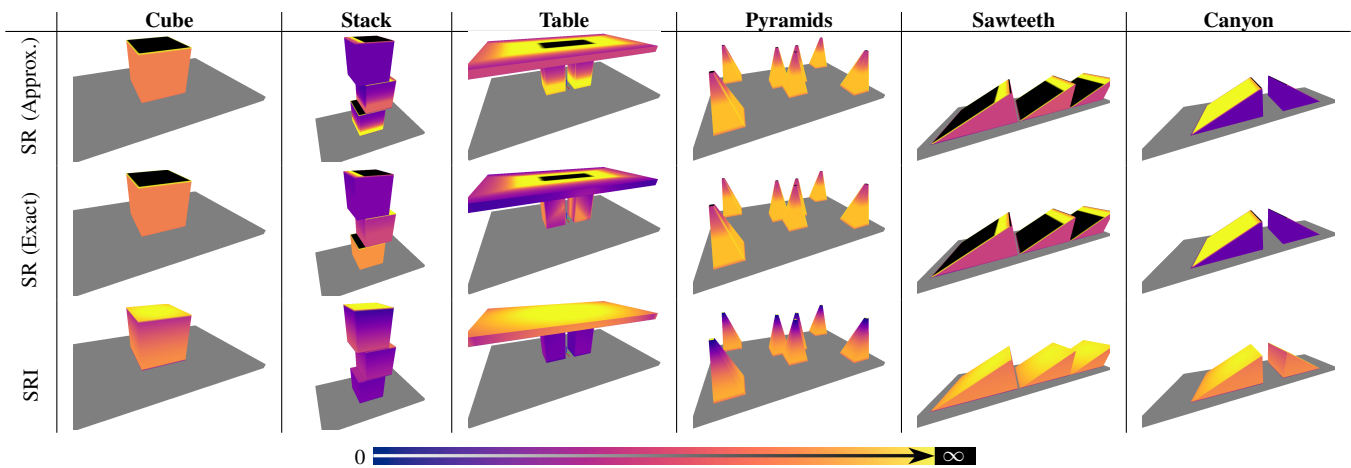


TABLE I: The six scenes used for the object placement planning experiments with the SR and SRI overlaid. The color of each point represents the SR/SRI value at that point with lighter colors indicating higher values and black indicating infinity.

B. Efficient Transportation

A mobile robot transporting a set of objects, while aiming to minimize the transportation time, should also avoid accelerating too quickly to prevent any object from being destabilized. Hence, determining the acceleration for which the assembly is on the verge of moving relative to the support — the maximal sustainable acceleration (MSA) — is key to ensuring the safety and efficiency of the transport. According to D’Alembert’s principle [48], an accelerating assembly can be treated as an equivalent static system, with a fictitious force applied at the center of mass in the direction opposite to the acceleration vector. The MSA of an assembly can be produced using Algorithm 2 by iterating over all connected sub-graphs (or super-objects) in the CIG and computing the MSA for all desired acceleration vectors. The super-object with the smallest MSA will be the first to move when the assembly is accelerated in the direction of the corresponding acceleration vector.

Our algorithm is showcased in Fig. 12, in which the MSA of two assemblies is computed for 100 acceleration vectors in the horizontal plane. The result from our algorithm is compared to the MSA computed using the dynamics simulation environment from [1], in which a mobile manipulator carries an assembly as shown in Fig. 2. The simulation experiments are performed with the PyBullet physics engine [49] at 900 Hz, and the contact error reduction parameter set to 0.2 for Fig. 12a and 0.15 for Fig. 12b. The MSA is assumed to be reached when a relative velocity of 0.05 m/s between objects in the assembly is exceeded. As shown in Fig. 12, the MSA computed using the simulator is in agreement with the MSA computed using our algorithm, with the latter being significantly faster does not require parameter tuning.

In the example pictured in Fig. 12a, the assembly can sustain a large acceleration in the $-Y$ direction (i.e. to the left) due to large coefficients of friction and due to the fact that the inertial force exerted on the cube will tend to push it against the slant and improve the contact conditions. At some point (i.e. 11.8 m/s^2), however, the inertial force will overcome the frictional forces and the assembly will slide to the right. In

comparison, a much smaller acceleration can be sustained in the $+Y$ direction (i.e. to the right) before the cube topples to the left under the influence of the inertial force. Adding a second cube behind the first one, as shown in Fig. 12b, prevents the first cube from toppling to the left and gives rise to a $2.5\times$ MSA increase in the $+Y$ direction, which can enable the robot to transport the assembly 63% faster if traveling in a linear motion. This comes at the cost of a MSA decrease in the $\pm X$ directions, as the second cube elevates the centre of mass of the assembly.

The MSA can be used to inform kinodynamic motion planners [50] on the maximal accelerations that can be safely reached by a mobile robot transporting an assembly [51, 52]. For instance, kinodynamic RRT* planners [53] and methods based on Bézier curve optimization [54] can use the MSA to ensure that the robot’s acceleration limits are respected while navigating the environment. Parallelized versions of these methods have been shown to be very fast [55, 56].

Algorithm 2: Maximal Sustainable Accelerations

input : CIG G , set of 3D acceleration directions \mathcal{D}
output: set of maximal sustainable accelerations \mathcal{X}

1. Initialize all $x_i \in \mathcal{X}$ to ∞
2. Define \mathcal{G} as the set of all connected sub-graphs in G

foreach $g_i \in \mathcal{G}$ **do**

3. Compute the mass m and centre of mass \mathbf{c} of g_i

foreach $\mathbf{d}_i \in \mathcal{D}$ **do**

4. Compute the robustness of g_i as $\text{SR}(\mathbf{c}, -\mathbf{d}_i)$
5. Compute the MSA with

$x_i \leftarrow \min \{x_i, \text{SR}(\mathbf{c}, -\mathbf{d}_i)/m\}$

VII. PLACEMENT PLANNING EXPERIMENTS

The benchmarking scenes from [11] were used to compare the performance of the algorithms proposed in this work to stably place a cube in an assembly of known objects. As shown in Table I, the scenes range from a simple cube resting on a flat surface to more complex assemblies that require reasoning

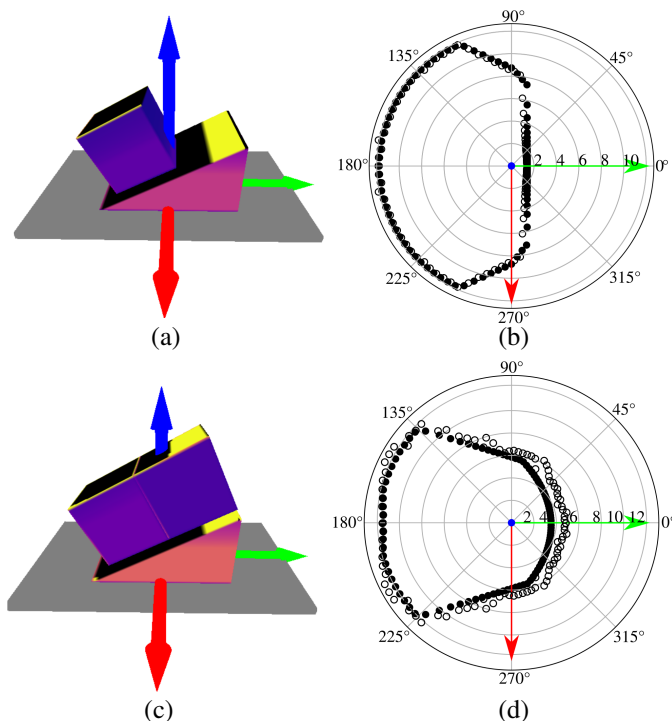


Fig. 12: The maximum sustainable acceleration (in m/s^2) of a structure in the $Z = 0$ plane (right side) when a single cube is on the slant (top), and when a second cube is placed behind the first one (bottom). Filled dots result from our algorithm while empty dots result from dynamics simulations.

about orientation or about using more than one object as support. For instance, a stable placement in the *Pyramids* scene requires making use of the three clustered pyramids to support the object, and the *Sawteeth* scene requires determining a pose with the right orientation. Similarly, the *Canyon* scene has two opposed slants with low coefficients of friction that are 1.6 m apart, leaving just enough space for the cube, whose edge length is 2 m, to be placed atop the two edges.

The approximate SR-based placement planning method proposed in [11] (SR-Approx) was used as a comparison point, reusing the original parameters but evaluating placements with the exact SR computation method proposed in this work. The exact counterpart (SR-Exact) to the approximate method was evaluated as a drop-in replacement by using the same parameters and methods as SR-Approx but with the exact SR map. The task was also performed from the SRI map using the sampling probability function in (57) with $\lambda = 0.995$ but otherwise using the same planning algorithm. Finally, our pose optimization technique (IPA) defined in Algorithm 1 was used in SRI+IPA, with a perturbation magnitude of $M = 0.1$ and $K = 15$ nearest neighbours, to refine the placement poses.

A total of 2400 experiments were performed across the six scenes and four methods, with the average evaluation criteria of each scene-method pair indicated in Table II. While the average time indicates the *effectiveness* of the planner (i.e. how quickly can an object be placed), the average number of iterations indicates the *efficiency* of the planner (i.e. its capacity to determine valid placements at each iteration). To evaluate the

		SR-Approx	SR-Exact	SRI	SRI+IPA
Cube	Time	0.387	0.41	0.356	0.888
	Iterations	3.35	3.63	2.69	1.65
	Med. SR	9.41	9.48	9.06	9.79
	Min. SR	2.43	2.45	1.98	3.5
	Volume	29.1	28.5	29.1	24.8
Stack	Time	2.28	1.95	1.12	1.45
	Iterations	7.52	6.22	2.87	1.72
	Med. SR	12.7	12.8	12.7	13.1
	Min. SR	1.85	2.14	1.91	2.57
	Volume	61.2	62.3	62.6	56.5
Table	Time	0.551	0.550	0.448	1.12
	Iterations	2.12	2.07	1.76	1.77
	Med. SR	4.9	4.87	4.92	5.18
	Min. SR	0.817	0.801	0.82	1.03
	Volume	100	98.9	98.0	98.3
Pyramids	Time	2.94	3.26	1.77	6.16
	Iterations	13.7	15.89	8.53	15.7
	Med. SR	4.97	5.03	4.98	5.56
	Min. SR	0.416	0.478	0.464	0.95
	Volume	143	139	139	140
Sawteeth	Time	2.43	2.73	4.07	4.6
	Iterations	6.16	7.34	12.3	5.24
	Med. SR	8.69	8.54	8.01	7.98
	Min. SR	1.53	1.64	1.47	1.99
	Volume	154	149	164	152
Canyon	Time	1.90	1.84	1.51	2.66
	Iterations	8.86	8.43	6.86	4.28
	Med. SR	5.63	5.78	5.64	5.26
	Min. SR	2.28	2.47	2.41	1.98
	Volume	126	129	121	119
Average Time		1.75	1.79	1.55	2.81
Average Min. SR		1.55	1.66	1.51	2.00

TABLE II: Average results from 2400 object placement planning experiments uniformly distributed across scenes and algorithms with time in sec., SR in N, and volume in m^3 .

quality of a placement, the median and minimum SR values of the resulting scene were computed, with the minimal SR being especially important as it indicates the weakest point in the assembly. Finally, the volume of the assembly bounding box was used to determine the compactness of the placement, a common motivation for object placement planning.

VIII. DISCUSSION

A. The Rigid Body Assumption Is No Silver Bullet

Although greatly simplifying kinematics, the rigid body assumption introduces its own set of challenges, such as the instantaneous transfer of forces across the assembly [57] and an infinite Young's modulus. In reality, objects will always deform slightly under the influence of forces, which is the basis of the contact force computation method in § IV-F. However, the friction direction constraint defined in § IV-C considers that infinitesimal displacements at the contact points must be consistent with the virtual motion of the whole object. Considering that an object can always slightly deform, the constraint in § IV-C should be relaxed to permit small deformations that are required for friction forces to arise. In practice, since most of the uncertainty in assembly robustness will probably come from estimates of the coefficient of friction and the pose of the objects, relaxing the constraint in § IV-C

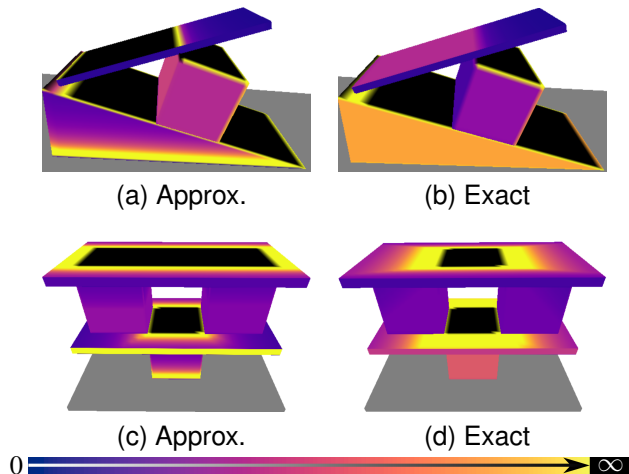


Fig. 13: By considering each object in isolation, the approximate SR method (left side) produces SR maps that can misguide the planner into selecting unstable placements. Our exact SR method (right side) can better guide the planner.

should have a limited impact on the accuracy of the SR map while simplifying the process of computing contact forces.

B. Approximate vs. Exact Static Robustness

While the approximate method proposed in [11] (SR-Approx) considers each object in isolation, the exact method proposed in this work (SR-Exact) considers the influence of every object in the assembly. This difference is reflected in the SR maps of assemblies whose CIG have a depth greater than one (e.g. the Stack and Table scenes in Table I). For instance, consider the scenes in Fig. 13, in which the SR-Approx method produced maps that mislead the planner into selecting unstable placements, thereby increasing the planning time. In Fig. 13b, the slab exhibits low SR values due to poor friction between the cuboid and the slant. This is not reflected in the approximate SR map of the slab in Fig. 13a since the reduced contact condition is not directly affecting it. Similarly, the scene in Fig. 13a-b can be easily toppled when placing weight above the top cubes, which is not reflected in the approximate SR map but is captured by the exact map.

Our exact SR method enabled the planner from [11] to produce valid placements 33% and 55% faster when performing placing experiments in the scenes at the top and bottom of Fig. 13, respectively. As a compromise between accuracy and computational complexity, the SR map could be computed for each object by considering only objects and interfaces within a limited distance in the CIG (e.g. within 4 edges), thereby relaxing the rigidity constraint and assuming that forces have a limited range of influence.

C. On Placement Planning Experiments

Our experiments show that the SRI+IPA method produces the most robust placements and does it in fewer iterations but at a higher computational cost. The increased robustness is attributed to our local pose optimization technique (IPA),

while the reduced number of iterations suggests that the SRI map enables more effective sampling of contact points. For instance, points at the bottom of the *Table* legs in Table I are likely to be sampled when SR-Approx is used, a problem that is mitigated when using SR-Exact or SRI. Moreover, points on the tabletop centre are more likely to be sampled with the SRI map than when using the SR map, resulting in greater robustness and fewer iterations. Compared to SR-Approx, our SRI+IPA algorithm achieved a 29% improvement in placement robustness, albeit at an increased compute cost. Finally, while using the exact SR map only provided a modest 7% robustness improvement in the benchmarked scenes, the example in Fig. 13 shows that the exact SR method can significantly reduce the planning time by avoiding the limitations of the myopic view inherent to the approximate SR method.

D. Limitations and Future Work

Although computing the exact SR offers significant advantages, it entails solving an NP-hard problem when determining contact forces [38]. Relaxing the non-linear constraints, as suggested in § VIII-A, could help mitigate this challenge. However, in the worst case, computing the robustness to toppling requires considering all combinations of objects in contact, making the computational complexity exponential with respect to the number of objects. As noted in § VIII-B, assuming that forces have a limited range of influence may mitigate this issue, though at the cost of reduced exactness.

Although our current approach assumes known rigid objects and no uncertainty in object pose, friction coefficient, or object shape, future work could consider propagating uncertainty from these factors into the SR map. This would enable the planner to select placements that are both robust and reliable. While our IPA algorithm significantly enhances placement robustness, the 80% increase in planning time suggests that improving the local pose optimization algorithm is a promising direction for future work. To further increase the planner’s efficiency, the contact point sampling method proposed in [11] and reused in this work could be refined to leverage information about previous attempts by avoiding sampling points close to previous points if they resulted in unstable placements. Lastly, while this work relied on either the SR or SRI maps, an algorithm integrating both could produce placements that improve the overall assembly robustness while respecting the maximal sustainable forces.

IX. CONCLUSION

In this work, we proposed a method to compute the robustness of an assembly to external forces, facilitating autonomous decision-making in tasks involving rigid objects in contact. Our method does not rely on heuristics or approximations, making it dependable in a broad range of scenarios involving multi-object assemblies. Although previous work has focused on respecting stability bounds, algorithms proposed herein can enable robots to reinforce structures and push the boundaries of assembly stability. We expect these methods to be valuable in various applications involving forceful interactions with the environment, such as efficient object transportation and safe, stable object placement.

REFERENCES

- [1] A. Heins and A. P. Schoellig, “Keep it upright: Model predictive control for nonprehensile object transportation with obstacle avoidance on a mobile manipulator,” *IEEE Robot. and Autom. Letters*, 2023.
- [2] F. G. Flores and A. Kecskeméthy, “Time-optimal path planning for the general waiter motion problem,” in *Advances in Mechanisms, Robot. and Design Education and Research*, pp. 189–203, Springer, 2013.
- [3] T. Omata and K. Nagata, “Rigid body analysis of the indeterminate grasp force in power grasps,” *IEEE Trans. on Robot. and Autom.*, vol. 16, no. 1, pp. 46–54, 2000.
- [4] Y. Maeda, K. Oda, and S. Makita, “Analysis of indeterminate contact forces in robotic grasping and contact tasks,” in *IEEE/RSJ Int. Conf. on Intelligent Robots and Systems*, pp. 1570–1575, 2007.
- [5] A. Bicchi and V. Kumar, “Robotic grasping and contact: A review,” in *IEEE Int. Conf. on Robot. and Autom.*, vol. 1, pp. 348–353, 2000.
- [6] F. Wang and K. Hauser, “Dense robotic packing of irregular and novel 3D objects,” *IEEE Trans. on Robot.*, vol. 38, no. 2, pp. 1160–1173, 2021.
- [7] K. Srinivas, S. Ganti, R. Parikh, A. Ahmad, W. Agboh, M. Dogar, and K. Goldberg, “The Busboy Problem: Efficient Tableware Decluttering Using Consolidation and Multi-Object Grasps,” in *IEEE Int. Conf. on Autom. Science and Engineering*, pp. 1–6, 2023.
- [8] Y. Jiang, M. Lim, C. Zheng, and A. Saxena, “Learning to place new objects in a scene,” *The Int. Journal of Robot. Research*, vol. 31, no. 9, pp. 1021–1043, 2012.
- [9] M. Wermelinger, R. Johns, F. Gramazio, M. Kohler, and M. Hutter, “Grasping and object reorientation for autonomous construction of stone structures,” *IEEE Robot. and Autom. Letters*, vol. 6, no. 3, pp. 5105–5112, 2021.
- [10] R. L. Johns, M. Wermelinger, R. Mascaro, D. Jud, I. Hurkxkens, L. Vasey, M. Chli, F. Gramazio, M. Kohler, and M. Hutter, “A framework for robotic excavation and dry stone construction using on-site materials,” *Science Robotics*, vol. 8, no. 84, p. eabp9758, 2023.
- [11] P. Nadeau and J. Kelly, “Stable Object Placement Planning From Contact Point Robustness,” [arxiv.org:2410.12483](https://arxiv.org/2410.12483), 2024.
- [12] F. Wang and K. Hauser, “Stable bin packing of non-convex 3D objects with a robot manipulator,” in *2019 Int. Conf. on Robot. and Autom.*, pp. 8698–8704, 2019.
- [13] L. Wang, S. Guo, S. Chen, W. Zhu, and A. Lim, “Two natural heuristics for 3D packing with practical loading constraints,” in *Pacific Rim Int. Conf. on Artificial Intelligence*, pp. 256–267, Springer, 2010.
- [14] Y. Lee, W. Thomason, Z. Kingston, and L. E. Kavraki, “Object reconfiguration with simulation-derived feasible actions,” in *IEEE Int. Conf. on Robot. and Autom.*, pp. 8104–8111, 2023.
- [15] H. Chen, W. Wan, K. Koyama, and K. Harada, “Planning to build block structures with unstable intermediate states using two manipulators,” *IEEE Trans. on Autom. Science and Engineering*, vol. 19, no. 4, pp. 3777–3793, 2021.
- [16] D. M. Saxena and M. Likhachev, “Planning for Complex Non-prehensile Manipulation Among Movable Objects by Interleaving Multi-Agent Pathfinding and Physics-Based Simulation,” in *IEEE Int. Conf. on Robot. and Autom.*, pp. 8141–8147, 2023.
- [17] J. E. Shigley, *Mechanical engineering design*. McGraw-Hill Companies, 1972.
- [18] P. R. Sinha and J. M. Abel, “A contact stress model for multifingered grasps of rough objects,” in *IEEE Int. Conf. on Robotics and Autom.*, pp. 1040–1045, 1990.
- [19] M. Otsuki and H. Matsukawa, “Systematic breakdown of Amontons’ law of friction for an elastic object locally obeying Amontons’ law,” *Scientific reports*, vol. 3, no. 1, p. 1586, 2013.
- [20] B. Bhushan, *Introduction to Tribology, Second Edition*. John Wiley & Sons, 2013.
- [21] B. Bhushan, “Contact mechanics of rough surfaces in tribology: multiple asperity contact,” *Tribology letters*, vol. 4, pp. 1–35, 1998.
- [22] C. Coulomb, *Théorie des machines simples: en ayant égard au frottement de leurs parties et à la roideur des cordages*. Bachelier, 1821.
- [23] R. Mattikalli, D. Baraff, and P. Khosla, “Finding all stable orientations of assemblies with friction,” *IEEE Trans. on Robot. and Autom.*, vol. 12, no. 2, pp. 290–301, 1996.
- [24] M. T. Mason, “Mechanics and planning of manipulator pushing operations,” *The Int. Journal of Robot. Research*, vol. 5, no. 3, pp. 53–71, 1986.
- [25] E. Whiting, H. Shin, R. Wang, J. Ochsendorf, and F. Durand, “Structural optimization of 3D masonry buildings,” *ACM Trans. on Graphics*, vol. 31, no. 6, pp. 1–11, 2012.
- [26] G. T.-C. Kao, A. Iannuzzo, B. Thomaszewski, S. Coros, T. Van Mele, and P. Block, “Coupled Rigid-Block Analysis: Stability-Aware Design of Complex Discrete-Element Assemblies,” *Computer-Aided Design*, vol. 146, p. 103216, 2022.
- [27] J. Yao, D. M. Kaufman, Y. Gingold, and M. Agrawala, “Interactive design and stability analysis of decorative joinery for furniture,” *ACM Trans. on Graphics*, vol. 36, no. 2, pp. 1–16, 2017.
- [28] H. V. Shin, C. F. Porst, E. Vouga, J. Ochsendorf, and F. Durand, “Reconciling elastic and equilibrium methods for static analysis,” *ACM Trans. on Graphics (TOG)*, vol. 35, no. 2, pp. 1–16, 2016.
- [29] D. E. Stewart, “Rigid-body dynamics with friction and impact,” *SIAM review*, vol. 42, no. 1, pp. 3–39, 2000.
- [30] C. K. Liu and D. Negrut, “The role of physics-based simulators in robotics,” *Annual Review of Control, Robotics, and Autonomous Systems*, vol. 4, no. 1, pp. 35–58, 2021.
- [31] T. G. Sugar and V. Kumar, “Metrics for analysis and optimization of grasps and fixtures,” in *IEEE Int. Conf. on Robot. and Autom.*, vol. 4, pp. 3561–3566, IEEE, 2000.
- [32] S. Lee and H. Moradi, “Disassembly sequencing and assembly sequence verification using force flow networks,” in *IEEE Int. Conf. on Robot. and Autom.*, vol. 4, pp. 2762–2767, 1999.

- [33] S. Lee and C. Yi, “Force-based reasoning in assembly planning,” in *Int. Design Engineering Technical Conferences and Computers and Information in Engineering Conference*, vol. 12877, pp. 165–172, 1994.
- [34] N. Boneschanscher, H. van der Drift, S. J. Buckley, and R. H. Taylor, “Subassembly stability,” in *AAAI Conf. on Artificial Intelligence*, vol. 88, pp. 780–785, 1988.
- [35] Y. Maeda, Y. Goto, and S. Makita, “A new formulation for indeterminate contact forces in rigid-body statics,” in *IEEE Int. Symposium on Assembly and Manufacturing*, pp. 298–303, 2009.
- [36] P. Nadeau, “A Standard Rigid Transformation Notation Convention for Robotic Research,” *arXiv preprint arXiv:2405.07351*, 2024.
- [37] J.-S. Pang and J. C. Trinkle, “Stability characterizations of fixtured rigid bodies with coulomb friction,” in *IEEE Int. Conf. on Robotics and Autom. (ICRA)*, vol. 1, pp. 361–368, 2000.
- [38] D. Baraff, “Issues in computing contact forces for non-penetrating rigid bodies,” *Algorithmica*, vol. 10, no. 2, pp. 292–352, 1993.
- [39] K. M. Lynch and F. C. Park, *Modern Robotics: Mechanics, Planning, and Control*. Cambridge University Press, 2017.
- [40] D. Stewart and J. C. Trinkle, “An implicit time-stepping scheme for rigid body dynamics with coulomb friction,” in *IEEE Int. Conf. on Robotics and Autom.*, vol. 1, pp. 162–169, 2000.
- [41] A. Wächter and L. T. Biegler, “On the implementation of an interior-point filter line-search algorithm for large-scale nonlinear programming,” *Mathematical programming*, vol. 106, pp. 25–57, 2006.
- [42] B. Siciliano, O. Khatib, and T. Kröger, *Springer handbook of robotics*, vol. 200. Springer, 2008.
- [43] R. Mojtahedzadeh, A. Bouguerra, E. Schaffernicht, and A. J. Lilienthal, “Support relation analysis and decision making for safe robotic manipulation tasks,” *Robot. and Autonomous Systems*, vol. 71, pp. 99–117, 2015.
- [44] F. S. Hillier and G. J. Lieberman, *Introduction to operations research*. McGraw-Hill, 2015.
- [45] A. Bicchi, “On the Closure Properties of Robotic Grasping,” *The Int. Journal of Robot. Research*, vol. 14, no. 4, pp. 319–334, 1995.
- [46] K. B. Petersen, M. S. Pedersen, *et al.*, *The matrix cookbook*. Technical University of Denmark, 2012.
- [47] W. Kabsch, “A solution for the best rotation to relate two sets of vectors,” *Acta Crystallographica*, vol. 32, no. 5, pp. 922–923, 1976.
- [48] H. Goldstein, C. Poole, and J. Safko, *Classical Mechanics, 3rd ed.* Addison Wesley, 2002.
- [49] E. Coumans and Y. Bai, “Pybullet, a python module for physics simulation for games, robotics and machine learning.” <http://pybullet.org>, 2016–2021.
- [50] B. Donald, P. Xavier, J. Canny, and J. Reif, “Kinodynamic motion planning,” *Journal of the ACM*, vol. 40, no. 5, pp. 1048–1066, 1993.
- [51] T. Kunz and M. Stilman, “Probabilistically complete kinodynamic planning for robot manipulators with acceleration limits,” in *IEEE/RSJ Int. Conf. on Intelligent Robots and Systems*, pp. 3713–3719, 2014.
- [52] S. M. LaValle and J. J. Kuffner Jr, “Randomized kinodynamic planning,” *The Int. Journal of Robot. Research*, vol. 20, no. 5, pp. 378–400, 2001.
- [53] D. J. Webb and J. Van Den Berg, “Kinodynamic RRT*: Asymptotically optimal motion planning for robots with linear dynamics,” in *IEEE Int. Conf. on Robot. and Autom.*, pp. 5054–5061, 2013.
- [54] B. Lau, C. Sprunk, and W. Burgard, “Kinodynamic motion planning for mobile robots using splines,” in *IEEE/RSJ Int. Conf. on Intelligent Robots and Systems*, pp. 2427–2433, IEEE, 2009.
- [55] B. Sundaralingam, S. K. S. Hari, A. Fishman, C. Garrett, K. Van Wyk, V. Blukis, A. Millane, H. Oleynikova, A. Handa, F. Ramos, *et al.*, “Curobo: Parallelized collision-free robot motion generation,” in *IEEE Int. Conf. on Robot. and Autom.*, pp. 8112–8119, 2023.
- [56] W. Thomason, Z. Kingston, and L. E. Kavraki, “Motions in microseconds via vectorized sampling-based planning,” in *IEEE Int. Conf. on Robot. and Autom.*, pp. 8749–8756, IEEE, 2024.
- [57] D. M. Kaufman, *Coupled principles for computational frictional contact mechanics*. PhD Thesis, Rutgers University Graduate School, 2009.
- [58] F. S. Hillier and G. J. Lieberman, *Introduction to operations research*. McGraw-Hill, 2015.

APPENDIX

A. Robustness Maximization

Slipping. Setting (37) to zero and solving for s produces the optimal magnitude

$$s = \left| \frac{\mu \hat{e}_n (\hat{e}_u \mathbf{f}_v - \hat{e}_v \mathbf{f}_u) \sqrt{-(\mu \hat{e}_n)^2 + \|\hat{e}_t\|^2}}{-(\mu \hat{e}_n)^2 \|\hat{e}_t\|^2 + \|\hat{e}_t\|^4} - \frac{\hat{e}_t^\top \mathbf{f}_t}{\|\hat{e}_t\|^2} \right| \quad (58)$$

where the positive root is taken to ensure a positive magnitude.

The second-order derivative of the contact condition with respect to s is

$$\frac{\partial^2 c}{\partial s^2} = \frac{-\|\hat{e}_t\|^2 \|\mathbf{f}_t + s \hat{e}_t\|^2 + (\hat{e}_t^\top (\mathbf{f}_t + s \hat{e}_t))^2}{\|\mathbf{f}_t + s \hat{e}_t\|^3} \quad (59)$$

in which the terms at the numerator are related with

$$\|\hat{e}_t\|^2 \|\mathbf{f}_t + s \hat{e}_t\|^2 \geq (\hat{e}_t^\top (\mathbf{f}_t + s \hat{e}_t))^2 \quad (60)$$

$$\|\hat{e}_t\| \|\mathbf{f}_t + s \hat{e}_t\| \geq \hat{e}_t \cdot (\mathbf{f}_t + s \hat{e}_t) \quad (61)$$

that is always true since $\mathbf{a} \cdot \mathbf{b} = \|\mathbf{a}\| \|\mathbf{b}\| \cos \theta$ with $-1 \leq \cos \theta \leq 1$. Both sides are equal when $\|\mathbf{f}_t\| = 0$ or $\|\hat{e}_t\| = 0$, in which case the critical point is at an inflection point. Otherwise, the critical point is a local maximum as the second-order derivative is negative. Four situations can be considered depending on the whether the solution to (58) is real or complex, and on the sign of the first-order derivative at $s = 0$, as summarized in Table III.

A complex solution to (58) is produced when $\|\hat{e}_t\|^2 < \mu^2 \|\hat{e}_n\|^2$, which makes the term under the square root in

(58) be negative. In this case, the contact condition is either monotonically increasing and $s^* = \infty$ or monotonically decreasing and $s^* = 0$. Finally, when the solution to (58) is real and the first-order derivative at $s = 0$ is positive, then $s^* = s$, otherwise $s^* = 0$.

s^*	$\frac{\partial c}{\partial s}(0) > 0$	$\frac{\partial c}{\partial s}(0) \leq 0$
$s \in \mathbb{R}$	(58)	0
$s \in \mathbb{C}$	∞	0

TABLE III: Magnitude of the external force that maximizes the contact condition at a given contact point as a function of the sign of the first-order derivative of the contact condition at $s = 0$ and the nature of the solution to $\partial c/\partial s = 0$.

In practice, finding the magnitude maximizing the contact condition can be done efficiently by proceeding in three steps:

- 1) If $\mu \hat{e}_n \leq \frac{\hat{e}_t^T \mathbf{f}_t}{\|\mathbf{f}_t\|}$, then $s^* = 0$.
- 2) Otherwise, if $\|\hat{e}_t\|^2 < \mu^2 \|\hat{e}_n\|^2$, then $s^* = \infty$.
- 3) Otherwise, s^* is given by (58).

In multi-object assemblies, the magnitude s^* of the external force \hat{e} maximizing the overall contact condition can be computed by considering the interfaces along the simple paths connecting \hat{e} to the fixed object in the CIG. Since $c(s)$ is always piecewise linear, as shown in Fig. 7, the sum of several such functions is also piecewise linear and has a maximum at one of the critical points [58]. Hence, the optimal magnitude of the external force that maximizes the overall contact condition can be obtained by (1) computing $s_i = \min(\text{SR}_{\text{slip}}, s^*)$ for each interface following the steps outlined previously, (2) computing the sum of contact conditions with (29) for each s_i , and (3) selecting the magnitude that maximizes the sum of contact conditions as the global optimal magnitude.

Toppling. Deriving the optimal magnitude of the external force that maximizes the force required to topple the object about all axes can be done in a similar fashion as for the contact condition, by setting the derivative of the objective function in (53) to zero and solving for s . With \mathbf{A} , \mathbf{b} and \mathbf{x} as defined in § V-F, setting (54) to zero and solving for \mathbf{x} produces the optimal magnitude

$$s^* = - \left(\mathbf{A}^T \mathbf{A} \right)^{-1} \mathbf{A}^T \mathbf{b} = - \frac{\mathbf{A}^T \mathbf{b}}{\|\mathbf{A}\|^2} \quad (62)$$

$$= - \frac{\sum_a^{\mathcal{A}} w_a \tau_a^g w_a \tau_a^e}{\sum_a^{\mathcal{A}} w_a \tau_a^e} \quad (63)$$

which maximizes the force required to topple the object about all axes in \mathcal{A} , the set of valid toppling axes in the assembly. The second-order derivative of the objective function in (53) with respect to s is given by

$$\frac{\partial}{\partial s} 2\mathbf{A}^T \mathbf{A} s - 2\mathbf{A}^T \mathbf{b} = 2\mathbf{A}^T \mathbf{A} = 2\|\mathbf{A}\|^2 \quad (64)$$

which is always positive, making s^* a global minimum.